Fully reconfigurable compact RF photonic filters using high-*Q* silicon microdisk resonators

Payam Alipour,[1] Ali Asghar Eftekhar,[1] Amir Hossein Atabaki,[1] Qing Li,[1] Siva Yegnanarayanan,[1,2] Christi K. Madsen,[3] and Ali Adibi[1,*]

[1]*School of Electrical and Computer Engineering, Georgia Institute of Technology, Atlanta, GA 30332, USA*
[2]*Currently with Lincoln Laboratory, Massachusetts Institute of Technology, Lexington, MA, 02420, USA*
[3]*School of Electrical and Computer Engineering, Texas A&M University, College Station, TX 77843, USA*
**adibi@ece.gatech.edu*

Abstract: We present a fully reconfigurable fourth-order RF photonic filter on SOI platform with a tunable 3-dB bandwidth of 0.9–5 GHz, more than 38 dB optical out-of-band rejection, FSR up to 650 GHz, and compact size (total area 0.25 mm^2). The center wavelength of the filter can be tuned over a wide range with a power consumption of 10 mW/nm. The filter architecture uses a unit-cell based approach to realize the desired filter specifications. The use of high-*Q* resonator-based components enables a dramatic reduction in size, weight and power (SWaP) of each unit cell, with the possibility of cascading a large number of these unit cells on a single chip. Thermal reconfiguration allows for low insertion loss and therefore results in the scalability of these filters. The demonstrated filter can be used in many different applications including RF photonic front-ends and high speed optical A/D conversion.

OCIS codes: (130.3120) Integrated optics devices; (130.7408) Wavelength filtering devices.

References and links

1. C. K. Madsen and J. H. Zhao, *Optical Filter Design and Analysis* (Wiley, 1999).
2. G. T. Reed and A. P. Knights, *Silicon Photonics: An Introduction* (Wiley, 2004).
3. R. A. Soref, "The past, present, and future of silicon photonics," IEEE J. Sel. Top. Quantum Electron. **12**(6), 1678–1687 (2006).
4. H. Rong, R. Jones, A. Liu, O. Cohen, D. Hak, A. W. Fang, and M. J. Paniccia, "A continuous-wave Raman silicon laser," Nature **433**(7027), 725–728 (2005).
5. A. W. Fang, H. Park, R. Jones, O. Cohen, M. J. Paniccia, and J. E. Bowers, "A continuous-wave hybrid AlGaInAs-silicon evanescent laser," IEEE Photon. Technol. Lett. **18**(10), 1143–1145 (2006).
6. Q. Xu, B. Schmidt, S. Pradhan, and M. Lipson, "Micrometre-scale silicon electro-optic modulator," Nature **435**(7040), 325–327 (2005).
7. A. Liu, L. Liao, D. Rubin, H. Nguyen, B. Ciftcioglu, Y. Chetrit, N. Izhaky, and M. J. Paniccia, "High-speed optical modulation based on carrier depletion in a silicon waveguide," Opt. Express **15**(2), 660–668 (2007).
8. T. Yin, R. Cohen, M. M. Morse, G. Sarid, Y. Chetrit, D. Rubin, and M. J. Paniccia, "31 GHz Ge n-i-p waveguide photodetectors on Silicon-on-Insulator substrate," Opt. Express **15**(21), 13965–13971 (2007).
9. L. Vivien, J. Osmond, J.-M. Fédéli, D. Marris-Morini, P. Crozat, J.-F. Damlencourt, E. Cassan, Y. Lecunff, and S. Laval, "42 GHz p.i.n Germanium photodetector integrated in a silicon-on-insulator waveguide," Opt. Express **17**(8), 6252–6257 (2009).
10. L. Schares, J. A. Kash, F. E. Doany, C. L. Schow, C. Schuster, D. M. Kuchta, P. K. Pepeljugoski, J. M. Trewhella, C. W. Baks, R. A. John, L. Shan, Y. H. Kwark, R. A. Budd, P. Chiniwalla, F. R. Libsch, J. Rosner, C. K. Tsang, C. S. Patel, J. D. Schaub, R. Dangel, F. Horst, B. J. Offrein, D. Kucharski, D. Guckenberger, S. Hegde, H. Nyikal, C.-K. Lin, A. Tandon, G. R. Trott, M. Nystrom, D. P. Bour, M. R. T. Tan, and D. W. Dolfi, "Terabus: Terabit/second-class card-level optical interconnect technologies," IEEE J. Sel. Top. Quantum Electron. **12**(5), 1032–1044 (2006).
11. A. Alduino, L. Liao, R. Jones, M. Morse, B. Kim, W. Lo, J. Basak, B. Koch, H. Liu, H. Rong, M. Sysak, C. Krause, R. Saba, D. Lazar, L. Horwitz, R. Bar, S. Litski, A. Liu, K. Sullivan, O. Dosunmu, N. Na, T. Yin, F. Haubensack, I. Hsieh, J. Heck, R. Beatty, H. Park, J. Bovington, S. Lee, H. Nguyen, H. Au, K. Nguyen, P. Merani, M. Hakami, and M. Paniccia, "Demonstration of a high speed 4-channel integrated silicon photonics WDM link with hybrid silicon lasers," in *Integrated Photonics Research, Silicon and Nanophotonics*, OSA Technical Digest (CD) (Optical Society of America, 2010), paper PDIWI5.

#148745 - $15.00 USD Received 6 Jun 2011; revised 22 Jul 2011; accepted 28 Jul 2011; published 4 Aug 2011

12. D. A. B. Miller, "Device requirements for optical interconnects to silicon chips," Proc. IEEE **97**(7), 1166–1185 (2009).
13. G. C. Valley, "Photonic analog-to-digital converters," Opt. Express **15**(5), 1955–1982 (2007).
14. J. Kim, M. J. Park, M. H. Perrott, and F. X. Kärtner, "Photonic subsampling analog-to-digital conversion of microwave signals at 40-GHz with higher than 7-ENOB resolution," Opt. Express **16**(21), 16509–16515 (2008).
15. J. Capmany, B. Ortega, and D. Pastor, "A tutorial on microwave photonic filters," J. Lightwave Technol. **24**(1), 201–229 (2006).
16. M. S. Rasras, K.-Y. Tu, D. M. Gill, Y.-K. Chen, A. E. White, S. S. Patel, A. Pomerene, D. Carothers, J. Beattie, M. Beals, J. Michel, and L. C. Kimerling, "Demonstration of a tunable microwave-photonic notch filter using low-loss silicon ring resonators," J. Lightwave Technol. **27**(12), 2105–2110 (2009).
17. S. S. Djordjevic, L. W. Luo, S. Ibrahim, N. K. Fontaine, C. B. Poitras, B. Guan, L. Zhou, K. Okamoto, Z. Ding, M. Lipson, and S. J. B. Yoo, "Fully reconfigurable silicon photonic lattice filters with four cascaded unit cells," IEEE Photon. Technol. Lett. **23**(1), 42–44 (2011).
18. E. J. Norberg, R. S. Guzzon, S. C. Nicholes, J. S. Parker, and L. A. Coldren, "Programmable photonic lattice filters in InGaAsP/InP," IEEE Photon. Technol. Lett. **22**(2), 109–111 (2010).
19. M. Soltani, S. Yegnanarayanan, and A. Adibi, "Ultra-high *Q* planar silicon microdisk resonators for chip-scale silicon photonics," Opt. Express **15**(8), 4694–4704 (2007).
20. A. Liu, L. Liao, D. Rubin, J. Basak, Y. Chetrit, H. Nguyen, R. Cohen, N. Izhaky, and M. J. Paniccia, "Recent development in a high-speed silicon optical modulator based on reverse-biased pn diode in a silicon waveguide," Semicond. Sci. Technol. **23**(6), 064001 (2008).
21. R. Patnaik, V. Vandrasi, C. K. Madsen, A. A. Eftekhar, and A. Adibi, "Comparison of cascade, lattice, and parallel filter architectures," J. Lightwave Technol. **28**, 3463–3469 (2010).
22. A. H. Atabaki, E. Shah Hosseini, A. A. Eftekhar, S. Yegnanarayanan, and A. Adibi, "Optimization of metallic microheaters for high-speed reconfigurable silicon photonics," Opt. Express **18**(17), 18312–18323 (2010).
23. S. Yegnanarayanan, P. D. Trinh, F. Coppinger, and B. Jalali, "Compact silicon-based integrated optic time delays," IEEE Photon. Technol. Lett. **9**(5), 634–635 (1997).
24. U. Fischer, T. Zinke, J.-R. Kropp, F. Arndt, and K. Petermann, "0.1 dB/cm waveguide loss in single-mode SOI rib waveguides," IEEE Photon. Technol. Lett. **8**(5), 647–648 (1996).
25. Q. Li, S. Yegnanarayanan, A. A. Eftekhar, and A. Adibi, "Low-loss microdisk-based delay lines for narrowband optical filters," in *Integrated Photonics Research, Silicon and Nano Photonics*, OSA Technical Digest (CD) (Optical Society of America, 2010), paper IMC7.
26. E. Shah Hosseini, S. Yegnanarayanan, A. H. Atabaki, M. Soltani, and A. Adibi, "Systematic design and fabrication of high-*Q* single-mode pulley-coupled planar silicon nitride microdisk resonators at visible wavelengths," Opt. Express **18**(3), 2127–2136 (2010).
27. C. W. Holzwarth, T. Barwicz, and H. I. Smith, "Optimization of hydrogen silsesquioxane for photonic applications," J. Vac. Sci. Technol. B **25**(6), 2658–2661 (2007).
28. A. H. Atabaki, A. A. Eftekhar, S. Yegnanarayanan, and A. Adibi, "Novel micro-heater structure for low-power and fast photonic reconfiguration," in *Conference on Lasers and Electro-Optics*, OSA Technical Digest (CD) (Optical Society of America, 2010), paper CWP6.
29. P. Dong, W. Qian, H. Liang, R. Shafiiha, N.-N. Feng, D. Feng, X. Zheng, A. V. Krishnamoorthy, and M. Asghari, "Low power and compact reconfigurable multiplexing devices based on silicon microring resonators," Opt. Express **18**(10), 9852–9858 (2010).

1. Introduction

In recent years, various optical filter systems have been proposed and demonstrated for a variety of applications [1]. In particular, integrated silicon-photonic filters can provide a low-cost and compact solution for reconfigurable optical filtering. The development of such filters has been in line with the vast expansion of the field of silicon (Si) photonics in the past decade [2,3]. With the demonstration of CW lasing [4,5] and the development of high-performance optical modulators [6,7] and optical detectors [8,9], the entire Si-photonic component toolbox is now available. Using such a toolbox, several academic research groups and companies are actively pursuing the development of Si-based optical interconnects [10–12].

There has been a parallel trend in the development of Si-photonic systems for analog signal processing. With the increasing demand for wideband wireless communication and ranging applications, the RF signal carriers have been pushed to higher and higher frequencies in order to achieve higher bandwidths. However, the speed and precision of wideband signal processing in the electronic domain is usually limited by the available sampling frequency (up to a few GHz) and the resolution of the analog-to-digital (A/D) converters [13,14]. In addition, the tuning range of electronic RF filters is limited by the RF carrier frequency [15].

#148745 - $15.00 USD Received 6 Jun 2011; revised 22 Jul 2011; accepted 28 Jul 2011; published 4 Aug 2011

Reconfigurable optical systems offer a solution to this challenge by providing low-loss and high-bandwidth filters that can be tuned over a wide frequency range [15]. By modulating an optical carrier with the RF signal and processing the modulated signal in the optical domain prior to digitization (as shown in Fig. 1), the RF photonics technology expands our ability to process wideband RF signals [15].

There have been several reports on the development of such filters on different platforms including silicon-on-insulator (SOI) [16,17] and indium phosphide (InP) substrates [18]. However, most of these filters are implemented by using long waveguides to achieve the required delay, which results in a relatively large footprint on the chip and small free spectral range (FSR) for the filter response. In this work, we present a fully reconfigurable filter unit cell on a CMOS-compatible SOI platform using compact delay line elements that are enabled by high-*Q* microdisk resonators [19]. The use of this resonator-based filter architecture results in a dramatic reduction in the size of the unit cell, and thus, the possibility of cascading a large number of these unit cells to achieve the desired filtering response over a very small footprint. We use the thermo-optic effect in Si to reconfigure the filter by thermal tuning, as opposed to tuning by free-carrier injection/depletion. The latter technique offers a faster response (<10 ns) [6,7], but has high and phase-dependent insertion loss (>1 dB per π phase shift) caused by free-carrier absorption [20] that limits the maximum tuning range of the filter. Since high speed is a key requirement for modulators, free-carrier-based methods have a clear advantage in implementing those devices. On the other hand, thermal tuning is a better option for reconfiguration purposes, especially when the number of reconfigurable elements is large, and the frequency of reconfiguration is not too high. The proposed filter architecture is discussed in Section 2, and its implementation is presented in Section 3. The experimental performance of these filters is demonstrated in Section 4, with more details discussed in Section 5. Final conclusions are presented in Section 6.

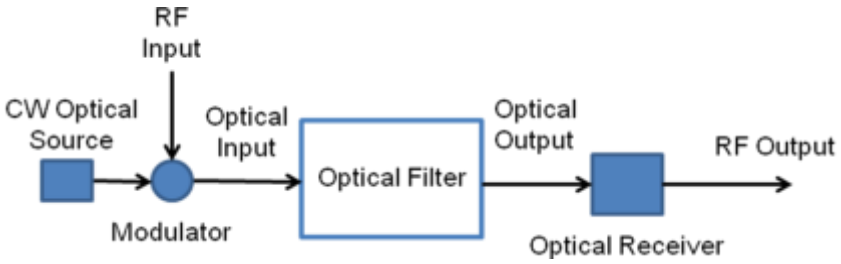

Fig. 1. Block diagram of an RF photonic filter system.

2. Filter Architecture

Our filter design technique is based on developing a fully reconfigurable unit cell as a basic low-order filter, and then combining multiple unit cells to implement higher-order filters. Each unit cell is a Mach-Zehnder interferometer (MZI) with a tunable single-pole, single-zero all-pass filter (APF) on each arm, and a constant phase term (β) on one of the arms [21]. The filter unit cell has two poles and two zeros. A schematic of the unit cell is depicted in Fig. 2, and an optical micrograph of the APF is shown in Fig. 3(a). The APF consists of a feedback loop (in this case, a racetrack resonator) that is coupled to the MZI arm using a tunable coupler. The tunable coupler itself is an MZI with a tunable phase shifter on one of its arms. The microdisk-based delay line is located on the feedback path. The thermally tunable phase shifters highlighted in the figure (i.e., φ_{MZI} and φ_{FB}) are metallic heaters optimally designed to locally heat a segment of a waveguide or a resonator [22]. The pole and zero of the APF are located at reciprocal locations with respect to the unit circle in the complex plane, as shown in Fig. 3(b). The phase (angle) of the APF pole is adjusted by changing the feedback phase shift

#148745 - $15.00 USD Received 6 Jun 2011; revised 22 Jul 2011; accepted 28 Jul 2011; published 4 Aug 2011

(φ_{FB}), while its magnitude is determined by the coupling coefficient of the tunable coupler (through φ_{MZI}) [21]:

$$\phi_{MZI} = 2\arcsin\left(\frac{|pole|}{\gamma}\right), \quad \phi_{FB} = -\angle pole \tag{1}$$

where γ is the amplitude response of the feedback loop (determined by the waveguide loss and the delay line loss), and the APF pole is given by $|pole|e^{j\angle pole}$ in the complex plane. The maximum achievable pole radius is therefore equal to γ. The transfer function of the unit cell is

$$G = -j\left[A_U + \exp(-j\beta)A_L\right]/2 \tag{2}$$

$$H = \left[A_U - \exp(-j\beta)A_L\right]/2 \tag{3}$$

where A_U and A_L are the transfer functions of the upper and lower APFs, respectively. The unit cell poles are identical to the poles of the two APFs; however, the locations of its zeros can be tuned independently by adjusting the input and output coupling ratios and β. This gives us full control over the placement of the unit cell poles and zeros, and therefore, full control

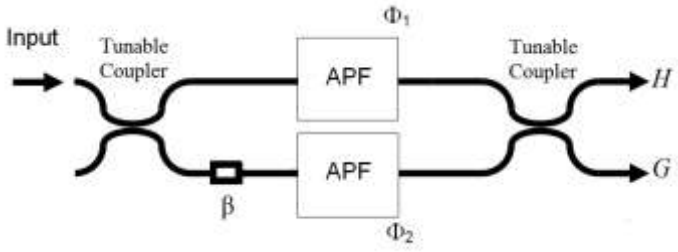

Fig. 2. Schematic of the filter unit cell. Each APF has one pole and one zero. β is a constant phase shift. H and G are the transfer functions of the unit cell in the upper and lower outputs, respectively.

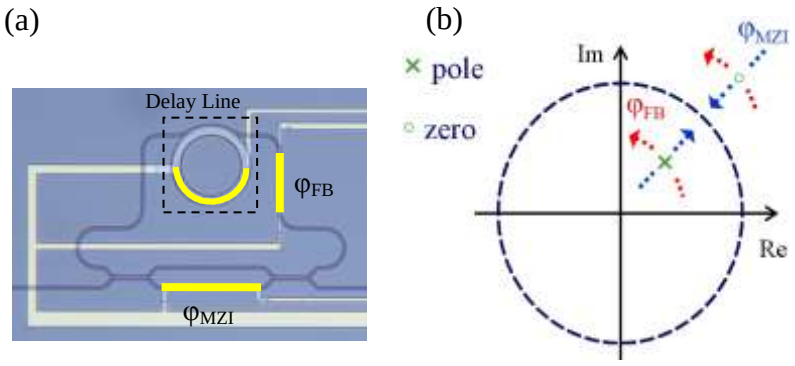

Fig. 3. (a) Optical micrograph of the APF located on each unit cell MZI arm in Fig. 2. The highlighted areas show the metallic heaters that are used to change the center frequency of the filter, as well as the feedback (φ_{FB}) and tunable coupler (φ_{MZI}) phase shifts. (b) The corresponding pole-zero diagram showing the simultaneous movements of the pole and zero as the phase shifters are tuned. The phase (angle) of the pole is adjusted by changing the feedback phase shift (φ_{FB}), while its magnitude is determined by the coupling ratio of the tunable coupler (through φ_{MZI}).

#148745 - $15.00 USD Received 6 Jun 2011; revised 22 Jul 2011; accepted 28 Jul 2011; published 4 Aug 2011

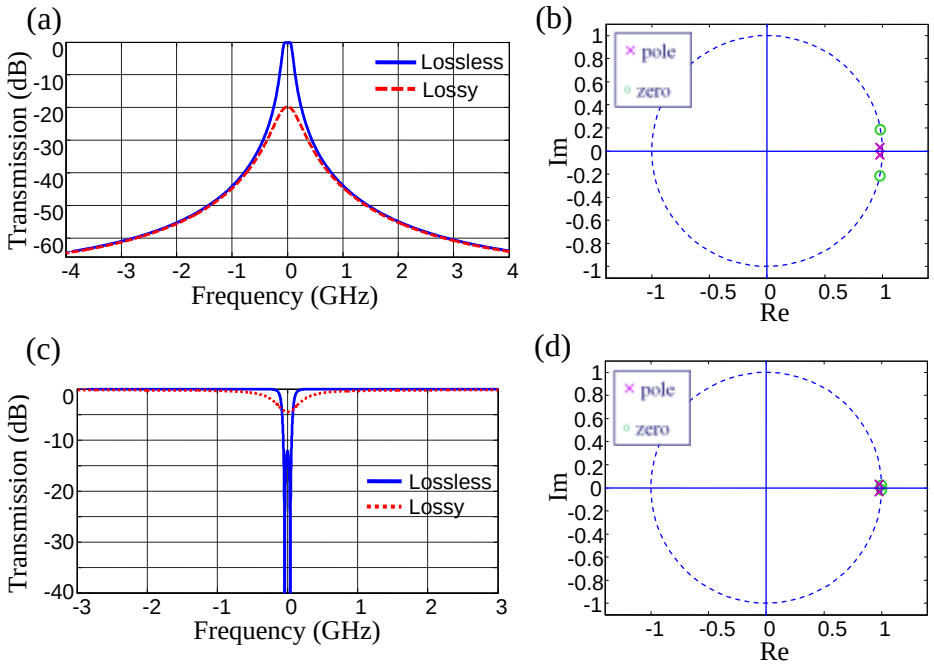

Fig. 4. (a) The blue (solid) curve is the simulated response of a lossless band-pass unit cell filter with $|pole|$ = 0.98, $\angle pole = \pm 0.026$, and $\beta = \pi$. It has a 3-dB bandwidth of 175 MHz. The red (dashed) curve is the response of the same filter when loss is added to the simulation. The added losses are 4.9 dB/cm for the waveguides and 0.7 dB/cm for the microdisk-based delay lines (see Section 3). The new 3-dB bandwidth is 325 MHz. (b) Pole-zero diagram for the lossless case in (a). (c) The blue (solid) curve is the simulated response of a lossless band-stop unit cell filter with $|pole|$ = 0.98, $\angle pole = \pm 0.026$, and $\beta = 0$. It has a 3-dB bandwidth of 175 MHz. The red (dotted) curve shows the response of the same filter when loss is added to the simulation. The new 3-dB bandwidth is 300 MHz. (d) Pole-zero diagram for the lossless case in (c).

over the bandwidth and the center frequency of the filter that can be configured as both FIR (band-stop) and IIR (band-pass) filters. For the filter response to be symmetric around the center frequency, the poles have to be complex conjugates of each other, and so do the zeros. Figure 4(a) shows the simulated response of a lossless band-pass unit cell filter with $|pole| = 0.98$, $\angle pole = \pm 0.026$, and $\beta = \pi$. The effect of adding loss to the simulation is also demonstrated in this figure. Figure 4(b) is the corresponding pole-zero diagram for the lossless case. By changing β from π to 0, the same unit cell will behave as a band-stop filter, as shown in Fig. 4(c). The corresponding pole-zero diagram for the lossless case is shown in Fig. 4(d).

Higher-order filters can be implemented by combining these unit cells in different ways, including baseline, cascade, and lattice architectures whose schematics are shown in Fig. 5. The baseline architecture has the lowest number of tunable elements. The cascade architecture is the easiest to design (since each stage can be designed and tuned independently) and has the largest out-of-band rejection. It is also the least sensitive to fabrication imperfections [21]. The lattice architecture has the smallest achievable bandwidth for a given maximum limit on the pole magnitude [21]. However, it is the most complex one in terms of design, characterization and reconfiguration. Considering all these factors, we believe that the cascade architecture is preferable to the other two. A fourth-order (i.e., four pole, four zero) filter can be realized by cascading two unit cells.

#148745 - $15.00 USD Received 6 Jun 2011; revised 22 Jul 2011; accepted 28 Jul 2011; published 4 Aug 2011

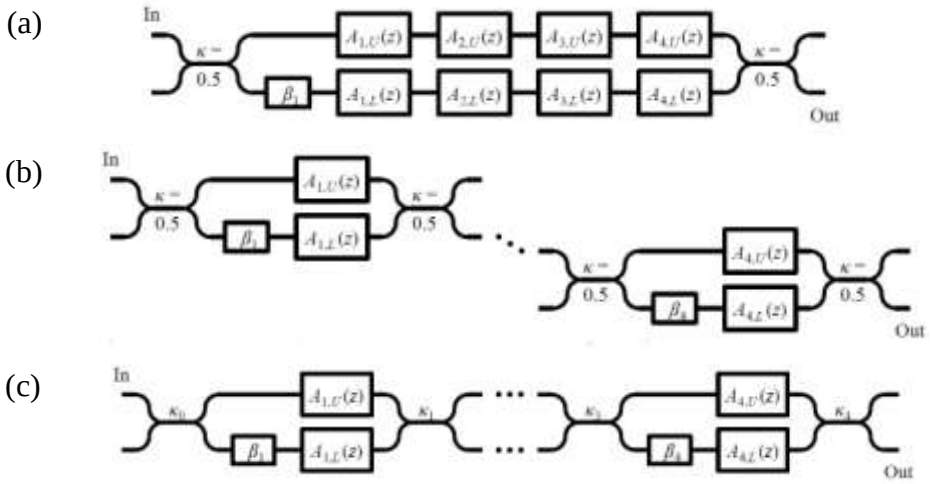

Fig. 5. Schematic of 8th-order (a) baseline, (b) cascade, and (c) lattice filter architectures. The smaller boxes represent phase shifters with constant phase shifts given by β_i. The larger boxes represent APFs with transfer functions given by $A_{i,U}(z)$ or $A_{i,L}(z)$. κ_i represents the power coupling coefficient between the two waveguides in the waveguide coupler.

3. Implementation

The filters are fabricated on an SOI wafer with a 230 nm thick Si device layer and a 1 μm thick buried-oxide (BOX) layer. Such thin SOI platforms enable devices that are more compact compared to their conventional rib-waveguide-based counterparts that are fabricated on thicker SOIs [23]. Compactness results in a smaller thermal capacitance, and therefore faster reconfiguration with less power consumption. However, waveguides fabricated on thin SOI have considerably more optical loss than rib waveguides do (e.g., 4.9 dB/cm for a 450 nm × 230 nm waveguide, compared to less than 1 dB/cm reported for rib waveguides [24]). Since the optical delay line is a critical element in our filter architecture, we need very low insertion loss delay lines. In this work, we break this trade-off between the device size and the insertion loss by using high-Q microdisk resonators (intrinsic Q ~1,000,000 corresponding to 0.7 dB/cm of loss) [19] to implement the delay elements. Our delay line is a 20 μm radius microdisk that is strongly coupled (i.e., over-coupled) to a bus waveguide [25] as shown in Fig. 6. Strong single-mode coupling between the waveguide and the microdisk is achieved through using a pulley (or concentric) coupling scheme [26]. The coupling Q is adjusted to be 30,000 in order to obtain a delay of 100 ps at the 1550 nm wavelength [25]. A detuning of ± 1 GHz around the resonance frequency results in a 10% reduction in the magnitude of the delay;

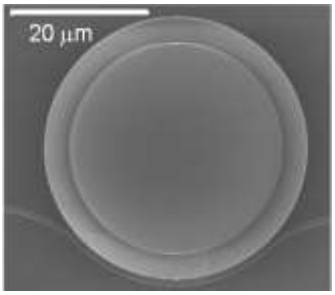

Fig. 6. SEM image of the delay line composed of a 20 μm radius microdisk resonator coupled to a 515 nm × 230 nm waveguide in the pulley coupling configuration. The gap between the waveguide and the resonator in the coupling region is 250 nm.

#148745 - $15.00 USD Received 6 Jun 2011; revised 22 Jul 2011; accepted 28 Jul 2011; published 4 Aug 2011

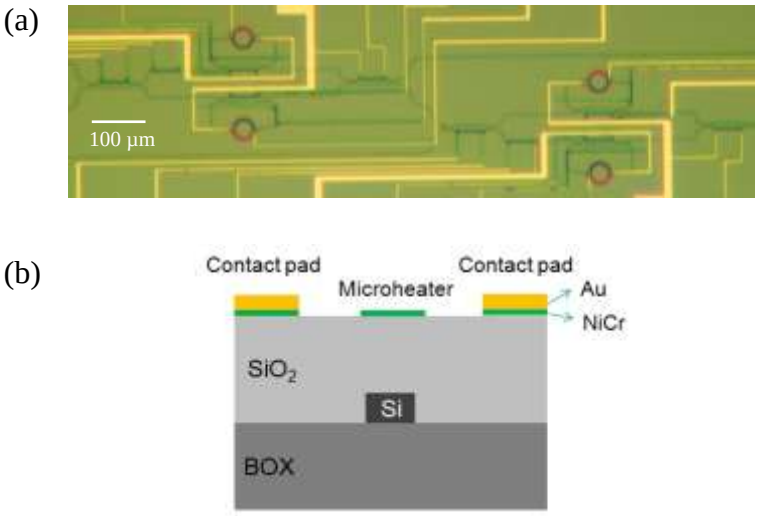

Fig. 7. (a) Optical micrograph of the fourth-order cascade filter implemented by cascading two second-order unit cells. (b) Cross-sectional schematic of the fabricated structure for a thermally reconfigurable device.

therefore, the maximum filter bandwidth is limited by the bandwidth of the delay line. Single-mode coupling means that the filter FSR can be as large as the FSR of the microdisk (~5.3 nm, or 650 GHz), which results in a broad spurious-free spectrum and also a large out-of-band rejection for band-pass filters. The above-mentioned values for the propagation loss and the coupling *Q* result in a maximum pole radius of ~0.92 for the filter unit cell.

The patterns are written on a layer of hydrogen silsesquioxane (HSQ) electron-beam (e-beam) resist using a JBX-9300FS e-beam lithography system. Dry etching is then performed in an inductively-coupled plasma (ICP) etching system with Cl_2 chemistry. Next, the devices are covered with a 1 μm thick SiO_2 layer using spin-on flowable oxide (FOx) that has superior uniformity and gap-filling properties when compared to deposited oxide films [27]. The patterns for the metallic elements are subsequently written on a layer of ZEP-520 e-beam resist that is spin-coated on top of the oxide cladding. After development, the sample is placed in an e-beam evaporation system and coated with a thin layer of titanium for surface adhesion, followed by layers of nichrome (NiCr alloy) and gold. Lift-off process is then used to complete this step. A third step of e-beam lithography with ZEP is used to define the microheater locations. After development, the sample is immersed in a liquid gold etchant to selectively remove the top gold layer. The high-resistance parts without the gold layer will act as microheaters, with the low-resistance parts forming the connections and the contact pads. The fabricated microheaters are 1 μm wide and 30–60 μm long. Figures 7(a) and 7(b), respectively, show an optical micrograph of a fourth-order cascade filter and a cross-sectional schematic of the fabricated structure.

4. Measurement results

To characterize the fabricated filters, the sample is placed on a thermally stabilized (0.01°C accuracy) stage. Light is coupled into and out of the sample using tapered optical fibers, and multi-contact probes are used to apply the tuning currents to the contact pads on the sample. The power consumption of each microheater is measured to be 20–30 mW per π phase shift. Figure 8(a) is the spectral response of the fourth-order cascade filter (Fig. 7(a)) in the band-pass configuration, with FSR ~650 GHz, a 3-dB bandwidth of 4–5 GHz, and an optical out-of-band rejection greater than 38 dB. Figure 8(b) is a close-up view of the area within the

#148745 - $15.00 USD Received 6 Jun 2011; revised 22 Jul 2011; accepted 28 Jul 2011; published 4 Aug 2011

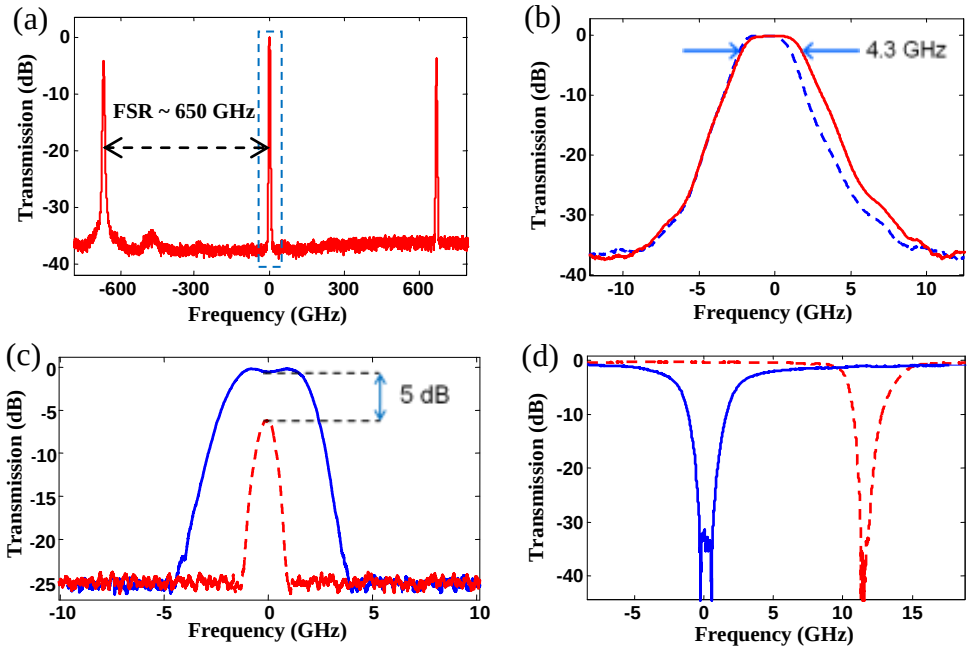

Fig. 8. (a) Band-pass filter response showing FSR ~650 GHz and out-of-band rejection > 38 dB. (b) Close-up view of the area within the dashed rectangle in (a). The 3-dB bandwidth of the red (solid) curve is 4.3 GHz. The blue (dashed) curve shows that the bandwidth can be fine-tuned without affecting the other parameters of the response. (c) Band-pass response with a different configuration. The 3-dB bandwidth is changed from 4 GHz (blue, solid curve) to 0.9 GHz (red, dashed curve). (d) Notch response with a null depth > 35 dB, obtained by reconfiguring the same filter. Comparison of the blue (solid) and red (dashed) curves shows that the center frequency and the bandwidth of the filter can be simultaneously tuned. The tuning of center frequency is achieved by shifting the center frequency of the delay line.

dashed rectangle in Fig. 8(a), showing a flat-top response whose bandwidth can be fine-tuned without affecting the other parameters of the response. A different band-pass response is shown in Fig. 8(c), with two different sets of filter parameters that result in 3-dB bandwidths of 4 GHz and 0.9 GHz. The insertion loss of the filter depends on the filter bandwidth: reducing the bandwidth from 4 GHz to 0.9 GHz increases the two-stage insertion loss from 2.5 dB to 7.5 dB (corresponding to 1.25 dB and 3.75 dB per stage, respectively). This additional 5 dB loss is a result of the increased photon traveling time in the APF as the MZI-racetrack coupling is reduced. Figure 8(d) shows that the same device can be reconfigured as a notch filter. Simultaneous tuning of center frequency and bandwidth is also demonstrated in this figure.

5. Discussion

The maximum achievable bandwidth for this filter is limited by the delay line bandwidth (10% reduction in the delay for a detuning of ± 1 GHz), while the minimum achievable bandwidth is limited by the delay line loss. Therefore, spectral resolution can be increased by reducing the resonator and waveguide losses through improving the fabrication quality, and possibly gain integration. An intrinsic microdisk *Q* of 5,000,000 would provide a spectral resolution better than 100 MHz for a single unit cell. These measures will also reduce the filter insertion loss. The total fiber-to-fiber insertion loss is mainly caused by the non-optimized coupling at the input and output facets and can be greatly reduced by improving the fiber-to-waveguide mode-matching.

#148745 - $15.00 USD Received 6 Jun 2011; revised 22 Jul 2011; accepted 28 Jul 2011; published 4 Aug 2011

Thermo-optic reconfiguration is preferable to free-carrier-based methods since it does not induce any additional optical loss, which, considering the number of tunable elements, can be significant especially for higher-order filters. There are nine microheaters per unit cell and each of them has a power consumption of 20–30 mW per π phase shift. However, the required phase shifts are typically much smaller than π. Hence, the average total tuning power per unit cell is about 100 mW. As for the reconfiguration time, the step response of the microheaters has a rise time of about 4 μs. We can use a pre-emphasis driver to reduce this to less than 1 μs [22]. Both the speed and the power consumption of reconfiguration can be further improved by one order of magnitude through using novel resonator-based phase shifters implemented with miniaturized microdisks (e.g., 2 μm radius) [28].

We have observed a thermal crosstalk of up to 5% between the microheaters. The effect of crosstalk can be compensated by measuring the crosstalk coefficients and considering them in the reconfiguration algorithm, so that the applied current for each microheater is adjusted accordingly. The crosstalk can be considerably reduced by etching deep micro-trenches around the heaters in order to thermally isolate them [29].

6. Conclusion

We have demonstrated a fully reconfigurable fourth-order (i.e., four-pole, four-zero) filter on thin SOI with a large FSR (~650 GHz), high out-of-band rejection (>38 dB optical), tunable bandwidth (0.9–5 GHz), and compact size (total area 0.25 mm^2). Full reconfigurability is achieved by using a flexible unit-cell based architecture with full control over the placement of poles and zeros. Optimally-designed microheaters are used to achieve fast reconfiguration (~1 μs) with low power consumption (<100 mW per unit cell). A major factor in facilitating the demonstrated performance is the use of high-*Q* microdisk resonators to realize compact and low-loss delay lines (0.7 dB/cm). Small SWaP (size, weight and power) enables the use of such filter chips in several systems applications in RF photonics including channelizers and LIDAR systems.

Acknowledgments

This work was supported by the DARPA Microsystems Technology Office (MTO) under grant No. 2106ATG as a part of the Si-PhASER program supervised by Dr. M. Haney and Dr. S. Rodgers.

#148745 - $15.00 USD Received 6 Jun 2011; revised 22 Jul 2011; accepted 28 Jul 2011; published 4 Aug 2011